Assessment of the Current Collection Quality of Pantograph-Catenary with Contact Line Height Variability in Electric Railways

Yang Song, *Member, IEEE*, Fuchuan Duan, *Member, IEEE*, Fanping Wu, Zhigang Liu, *Senior member, IEEE*, Shibin Gao

***Abstract*— The numerical tools are widely used to facilitate the design of the railway catenary. Only radical results are obtained as the current assessment is generally performed without any practical errors. In this paper, the most common error, the contact line height variability, is appropriately included in evaluating the current collection quality. Based on the real-life contact line height data collected from a high-speed network, the heights of the key points in the contact line are extracted, of which the pointwise stochastics is represented by the PSD function. Random samples are generated by the inverse Fourier transform based on the Monte Carlo method. An advanced initialisation procedure is presented to properly include the contact line height variability in the initial configuration. A stochastic analysis with a high cut-off frequency is performed to evaluate a double pantographs-catenary system's current collection quality. Unlike the deterministic result obtained by the perfect design data, the contact line height variability causes uncertainty. The present analysis method indicates some risks of safety accident and contact loss which the traditional simulation cannot capture with ideal design data or low cut-off frequency.**

***Index Terms*— Electric Railway; Catenary; Pantograph; Current Collection Quality; Contact Line Height Variability; Stochastic Analysis**

I. Introduction

n electric railways, the catenary constructed along the railroad Iis used to provide continuous electric current for the locomotive via pantographs mounted on the carbody's roof. As a crucial part of the traction power system [1], the sliding contact performance between the pantograph and the catenary directly determines the current collection quality. A deteriorated contact quality of the pantograph-catenary mainly reflects in an incremental fluctuation in the contact force. An overlarge contact force causes extra stress and wear in the pantograph strip [2] and the contact line [3] and reduces the system's life expectancy. An inadequate contact force increases the probability of arcing occurrence, which may burn the contact surface and cause electric transmission issues [4], [5]. Therefore, good contact quality is desired to enable a fast and safe train without traffic disorders.

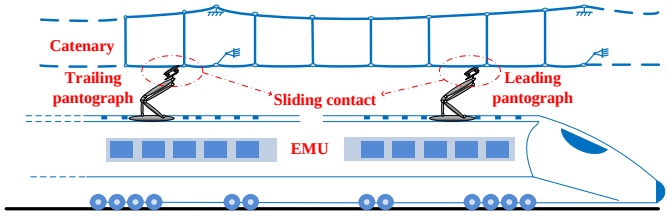

Figure 1. Schematic of a pantograph-catenary system

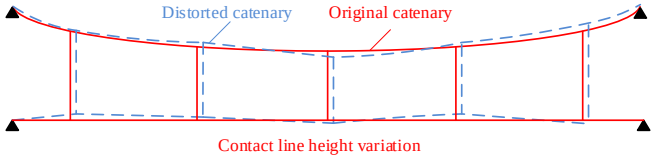

Figure 2. Illustration of the distorted catenary system

The pantograph-catenary contact quality is challenged by multiple disturbances from the vehicle-track excitation [6], the unfriendly working conditions [7] and the anomaly of the catenary and pantograph [8]. A few previous researchers have devoted their attention to the research of the pantograph-catenary interaction, and many new techniques have been developed for achieving better current collection quality. To efficiently reproduce realistic pantograph-catenary behaviours, various types of mathematical models have been developed [9], which were usually used in the design phase to check the design strategy's acceptance. Primarily, the numerical simulations were performed with the perfect design data, which could only reproduce the pantograph-catenary response in the ideal condition [10]. Recently, the study of pantograph-catenary dynamics with external perturbations has attracted the ever-

Manuscript received xxxx; revised xxxx; accepted xxxx. Date of publication xxxx; date of current version xxxx. This work was supported in part by the National Natural Science Foundation of China (U1734202). (Corresponding author: Fuchuan Duan)

Yang Song is with the Department of Structural Engineering, Norwegian of Science and Technology, Trondheim, 7491, Norway. (e-mail: y.song_ac@hotmail.com).

Fuchuan Duan is with the Institute of Rail Transit, Tongji University, Shanghai, 201804, China. He is also with the School of Electrical Engineering, Southwest Jiaotong University, Chengdu, 610031 China (email: duanfc_cd@outlook.com).

Fanping Wu, Zhigang Liu and Shibin Gao are with the Electrical Engineering Department, Southwest Jiaotong University, Chengdu, 610031 China. (e-mail: wufanping123@163.com, liuzg_cd@126.com, gao_shi_bin@126.com)

increasing interest of several scholars. The wind farm along the catenary was constructed to study the wind-induced vibration [11], and its effect on the pantograph-catenary interaction was investigated [12]. The pantograph-catenary arcing in abnormal operation conditions was detected in a laboratory test via high-resolution photography [13]. Apart from the physical models, the data-driven method was another practical approach to predict and assess pantograph-catenary performance. Using the catenary trip fault data from China high-speed network, a risk index system was established considering the characteristics of time-space differences [14]. Much previous research focusing on the detection and identification of the catenary anomalies were reported in [15]–[17], of which the effect was seldom included in the assessment of pantograph-catenary interaction performance. In [18], an image processing-based monitoring and fault diagnosis for the pantograph-catenary interaction is proposed and validated experimentally. In [19], [20], the defective dropper is introduced in the finite element model of catenary, and its effects on the initial configuration and the interaction performance are quantified.

In real-life operations, the contact line cannot always be flat as designed in ideal conditions. The long-term service, mounting errors, and inadequate maintenance result in the catenary's geometrical distortion with respect to its original design geometry, as shown in Figure 2. In [21]–[23], the effect of contact line irregularities was introduced in the mathematical modelling of a catenary. However, only the basic assessment was conducted via the contact force filtered within 0-20 Hz in these works. Especially in [22], [23], a cable element could not capture the pantograph-catenary's high-frequency behaviour. The assessment indices used in [22], [23] only reflected the comprehensive performance instead of local and transient behaviours. The scientific community has recognised that most unsatisfactory behaviours (such as contact loss and overlarge maximum contact force) primarily happened at high frequency. Therefore, the assumption is desired to be improved, and a nonlinear beam element should be used to describe the catenary's high-frequency behaviour [24] entirely. In [24], the catenary's geometry deviation was included in the catenary model to assess the pantograph-catenary interaction performance. Nevertheless, the target configuration cannot be ensured to be the same as reality as the measurement geometry was not provided. In [25], an inverse model was presented to include the measurement geometry deviation. The high-frequency behaviour is desired to be investigated with double pantograph operations. In real-life operations, the high-speed train is frequently equipped with double pantographs to increase the carrying capability, as shown in Figure 1. The trailing pantograph has a lousy performance typically due to the disturbance of the wave propagation from the leading pantograph [26], which also cannot be described in the previous works in [21], [22]. Another significant effect of the contact line height variation is introducing stochastic disturbances to the pantograph-catenary interaction and leading to indeterministic behaviours, which is similar to the random effect of track profile corruptions on the carbody vibration [27]. Some researches have been conducted to monitor the evolvement of the track profile [28] and investigate its random effect on the dynamic response of the high-speed train [29] and the maglev system [30]. Similarly, the contact line is the pantograph's slideway, and the contact line variability directly affects the vertical contact with pantographs. Due to the stochastic nature of the contact line height, the traditional deterministic assessment approaches may not evaluate the current collection quality with random excitations. The stochastic analysis is desired to be performed using numerical tools with the proper inclusion of the realistic contact line height variability.

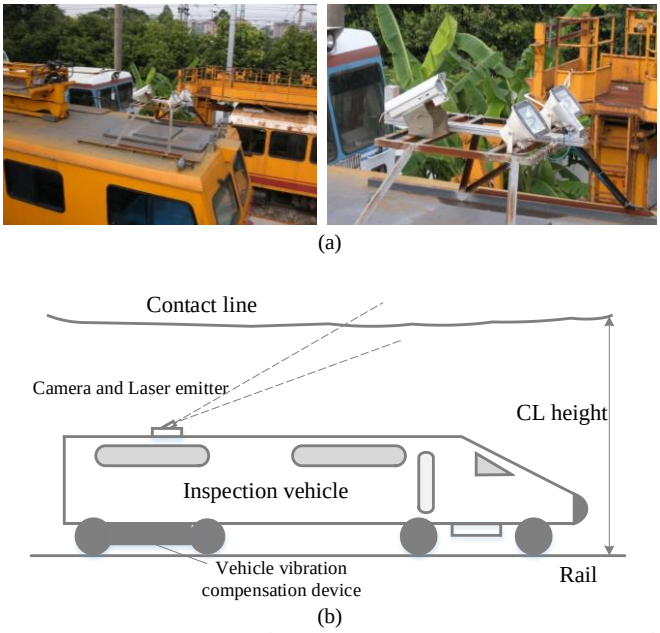

Figure 3. Inspection vehicle for catenary static parameters: (a) Real-life inspection vehicle; (b) Schematics of non-contact measurement

The above issues are addressed in this paper to evaluate the current collection quality with the contact line height variability. The contact line height's measurement data is collected from the China high-speed network by an inspection vehicle. The dropper and steady arm points in the contact line are extracted from the measurement data. Their statistical distribution is described by the power spectrum density (PSD) function. A nonlinear finite element model of the catenary with contact line height variability is developed to simulate the high-frequency response excited by double pantographs. The pantograph-catenary system's current collection quality is evaluated with the random realistic contact line height instead of the ideal conditions in previous works through stochastic analysis.

II. Description of Measurement Data

The contact line height data used in this work are collected from the China high-speed network through a non-contact inspection vehicle, as shown in Figure 3, which regularly runs to monitor the catenary's static parameters and assess the health status of the catenary. The contact line height can be calculated according to the time spent in the laser transmitting from the emitter to the camera, corrected with the inspection vehicle's vibration compensation. The measured vertical contact line height is presented in Figure 4, in which the measurement noise has been removed through pre-processing. The droppers and steady arms support the contact line. Therefore, the contact line's shape is directly determined by the position of key points

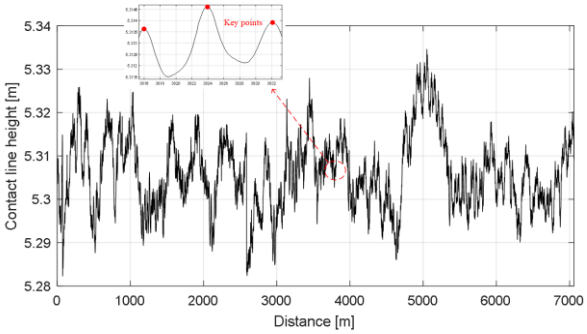

Figure 4. Measurement data of contact line height

(dropper and steady arm points). The deformation of the contact line between any two adjacent key points is purely caused by gravity. It can be seen from the locally enlarged view in Figure 4 that the three key points are denoted by the red dots. In the next section, a procedure is proposed to extract the key points from the measurement data, and the representation of the pointwise stochastics is discussed.

III. Stochastic Representation of Contact Line Height Variability

This section presents a procedure to extract the dropper and steady arm points in the contact line from the measurement data. From the locally enlarged view in Figure 4, it is seen that the key points are always on the top of the sag caused by gravity. Thus, the upper envelope can be used to capture all the information of the key point height from the measured contact line height. The procedure to extract the key points has two steps as follows:

Step 1, Upper envelope extraction

Here the Hilbert transformation is employed to extract the upper envelope from the measured contact line height [31]. Applying the direct discrete Fourier transform (DFT) to the measured contact line height $z(n)$ yields

$$Z_k(n)=\frac{1}{N}\sum_{n=0}^{N=1} z(n)\exp\left(-j\frac{2\pi kn}{N}\right) \tag{1}$$

in which n is the integer from 1 to N. $Z_k(n)$ is the spectrum of the original signal. The Hilbert signal $\tilde{Z}(n)$ can be expressed by:

$$\tilde{Z}(n)=z(n)+j\hat{Z}(n) \tag{2}$$

where $\hat{Z}(n)$ is the Hilbert transform in the frequency domain of $z(n)$, which can be defined in the following form:

$$\tilde{Z}(n)=\sum_{k=0}^{N-1} V_k \exp\left(j\frac{2\pi kn}{N}\right)$$
$$V_k=\begin{cases}-jZ_k(n), & \text{where } k=1\sim(N/2-1)\\ Z_k(n)=0, & \text{where } k=0;\ k=N/2\\ jZ_k(n), & \text{where } k=(N/2+1)\sim(N-1)\end{cases} \tag{3}$$

The upper envelope can be determined by calculating the amplitude of $\tilde{Z}(n)$ as

$$A(n)=\sqrt{z^2(n)+\hat{Z}^2(n)} \tag{4}$$

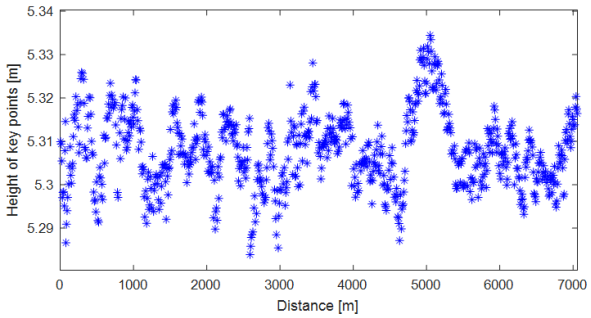

Figure 5. Key points extracted from measurement data

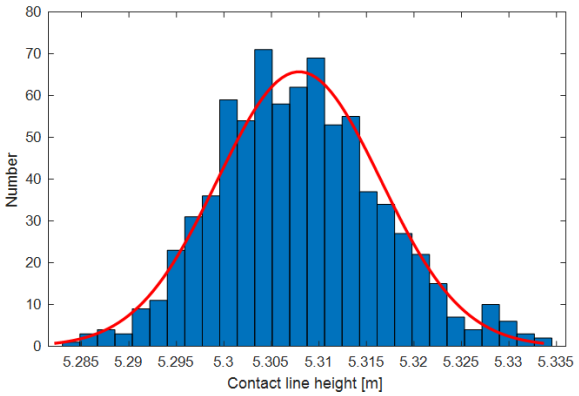

Figure 6. Histogram and fitted normal density function of key points

Step 2, Intersection points calculation

The key points are the intersection points between the original signal $z(n)$ and the envelope $A(n)$. The vertical positions of key point $P(m)$ can be determined by

$$P(m)=A(n), \quad \text{if } A(n)=z(n) \tag{5}$$

The key points extracted from the measurement data are presented in Figure 5. It is seen that these key points show evident spatial stochastics. The histogram and the fitted normal density function of key points are presented in Figure 6. It is seen that these key points follow a symmetric distribution with respect to its mean 5.308 m, which is very close to the design height of 5.3 m. The extra 0.008 m can be compensated by slightly increasing the pantograph's working height during the operation, which has no contribution to the contact force fluctuation. The symmetric distribution indicates a stationary process of the key point which is expected to exhibit a periodicity relevant to the span length. Therefore, the stationary random process's frequency characteristics can be represented by the PSD function, as shown in Figure 7. The peaks of span length and half span length can be observed.

The measured PSD in Figure 7 can be used to generate the random time-histories of key points for the numerical analysis via the inverse Fourier transform. Firstly, the unilateral spectrum in Figure 8 is converted into a bilateral spectrum $S_p(f)$. According to Ref. [27], the spectrum modulus of the time-domain sequence can be expressed by

$$|X(k)|=\sqrt{N_r^2\times S_p(k)}=N_r\sqrt{S_p(k\Delta f)\Delta f}\quad (k=0,1,\ldots,N_r-1) \tag{6}$$

in which N_r is the number of sampling points. As $X(k)$ is a random process, the spectrum phase $\xi(k)$ is assumed as follows with random φ distributing uniformly between 0 and 2π.

$$\xi(k) = \cos\varphi(k) + i\sin\varphi(k) \tag{7}$$

Thus, $X(k)$ can be obtained as

$$X(k) = \xi(k)\left|X(k)\right| = N_r\,\xi(k)\sqrt{S_p(k\Delta f)\Delta f} \quad (k = 0,1,\ldots,N_r/2) \tag{8}$$

It should be noted that the real and imaginary parts of $X(k)$ are even and odd symmetric with respect to $N_r/2$. The spectrum modulus on $(N_r/2+1)\sim N_r$ can be obtained by conjugating $X(k)$ on $0\sim N_r/2$. Through the Inverse Fourier transform to $X(k)$, the time-history $\gamma(n)$ can be generated as follows:

$$\gamma(n) = \frac{1}{N_r}\sum_{k=0}^{N_r-1} X(k)\cdot e^{i2\pi kn/N_r},\ n\in[0,N_r-1] \tag{9}$$

To implement a stochastic analysis of the current collection quality with the uncertainties of contact line height, the Monte Carlo technique is taken to produce several samples based on the measured PSD. The Monte Carlo method's advantage is to take the nonlinearities and uncertainty of the model into account without imposing any restrictions on the output probability distributions. However, many numerical simulations are required to ensure accuracy, which entails a tremendous computational cost. In [32], it has been proven that a tiny element length should be used to avoid the contamination of the numerical results at high frequencies, which consumes enormous computational resources. Thus, in this analysis, a reasonable number of samples is selected as 500 to quantify the uncertainties of the current collection quality caused by the contact line height variability. Figure 8 (a) presents 500 generated time-histories of key point height from the measured PSD. The comparison of the generated PSDs against the measured one is presented in Figure 8 (b). It is seen that the generated PSDs show good consistency with the measured one. Some crucial frequency components like the span length, half span length can be well described in the generated PSDs. According to the spatial position of key points in the real world, their heights can be extracted from the generated signals $\gamma(n)$ in Figure 8 (a) by interpolation.

IV. Modelling of Pantograph-Catenary with Contact Line Height Variability

The catenary modelling techniques have experienced significant development in the past decade, as summarised in [33]. A nonlinear finite element approach is adopted to represent the catenary model in this work to describe the initial configuration and address the intrinsic nonlinearity accurately. The catenary is modelled by ANCF, and the pantograph is represented by a widely-used lumped mass model. The TCUD (target configuration under dead loads) method is employed to compute the catenary's initial configuration, including the contact line height variability.

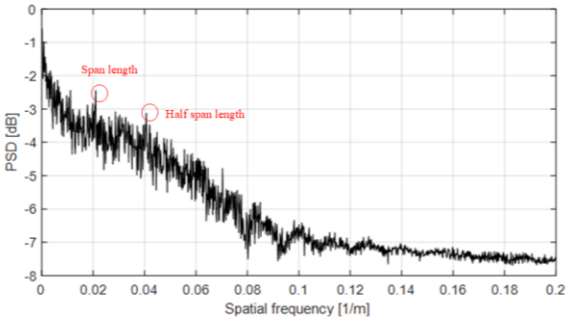

Figure 7. PSD of measured key points

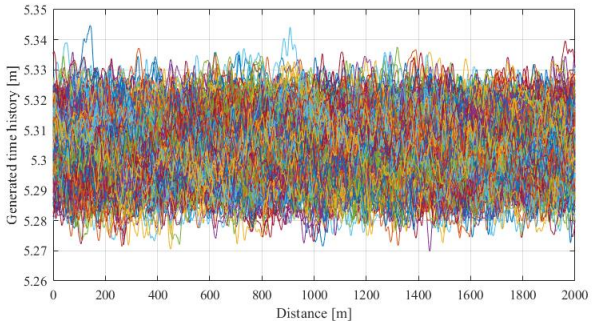

(a)

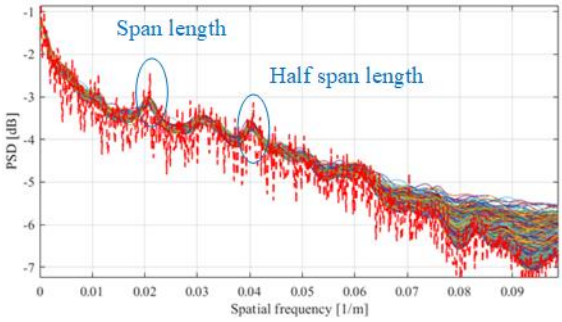

(b)

Figure 8. Generated key point height from measured PSD: (a) Time-histories; (b) PSD comparison
(Red dash line denotes the measurement PSD and others denote the generated PSD)

A. ANCF beam and cable elements

The catenary is generally comprised of five types of components: the contact line, the messenger line, the dropper, the stitch line and the steady arm, as illustrated in Figure 9. The contact line is used to carry the electrical current to be collected by pantographs. The messenger line and droppers are used to hang the contact line, keeping it at the designing height. The stitch lines are customarily installed to reduce the elasticity unevenness. To adequately describe the geometrical nonlinearity of the messenger/contact/stitch lines, the ANCF beam element is employed. The dropper's slackness is described by an ANCF cable element that can only withstand the tension but not compression. A linear truss element is used to model the steady arm. The claws on clamps in the droppers, steady arms and stitch lines are assumed as lumped masses.

In this work, the ANCF beam with 12 degrees of freedom (DOFs) that contains the displacements and the gradients is

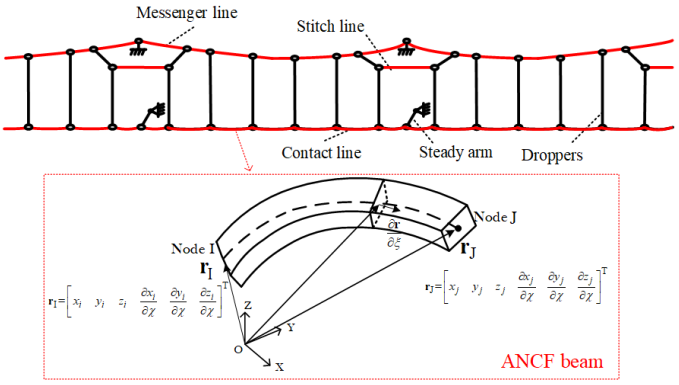

Figure 9. A catenary model with ANCF beam element

adopted to model the catenary. The DOF vector for one element is defined as follows:

$$\mathbf{e}=\left[\begin{array}{cccccccccccc} x_i & y_i & z_i & \frac{\partial x_i}{\partial \chi} & \frac{\partial y_i}{\partial \chi} & \frac{\partial z_i}{\partial \chi} & x_j & y_j & z_j & \frac{\partial x_j}{\partial \chi} & \frac{\partial y_j}{\partial \chi} & \frac{\partial z_j}{\partial \chi} \end{array}\right]^{\mathrm{T}} \tag{10}$$

in which χ is the local coordinate from 0 to the element length L_0. The position vector in the deformed configuration $\mathbf{r}$ is calculated by the product of $\mathbf{e}$ and the shape function matrix $\mathbf{S}$ as

$$\mathbf{r}=\mathbf{S}\mathbf{e} \tag{11}$$

where $\mathbf{S}$ can be defined as follows:

$$\mathbf{S}=\left[\begin{array}{cccccccccccc} S_1 & & & S_2 & & & S_3 & & & S_4 & & \\ & S_1 & & & S_2 & & & S_3 & & & S_4 & \\ & & S_1 & & & S_2 & & & S_3 & & & S_4 \end{array}\right]$$

$$\begin{aligned} S_1(\xi)&=1-3\xi^2+2\xi^3 \\ S_2(\xi)&=L_0\left(\xi+\xi^3-2\xi^2\right) \\ S_3(\xi)&=3\xi^2-2\xi^3 \\ S_4(\xi)&=L_0\left(\xi^3-\xi^2\right) \end{aligned} \tag{12}$$

The strain energy can be assumed to be the summation of the contributions of axial and bending deformation, which is calculated by

$$U=\frac{1}{2}\int_0^{L_0}(EA\varepsilon_l^2+EI\kappa^2)d\chi \tag{13}$$

in which E is Young's modulus, A is the section area, I is the moment inertial of the wire, ε_l is the longitudinal strain and κ is the curvature. ε_l and κ can be obtained as follows:

$$\begin{aligned} \varepsilon_l&=\frac{1}{2}\left(\mathbf{r}_\chi\mathbf{r}_\chi-1\right) \\ \kappa&=\frac{\left|\mathbf{r}_\chi\times\mathbf{r}_{\chi\chi}\right|}{\left|\mathbf{r}_\chi\right|^3} \end{aligned} \tag{14}$$

in which

$$\begin{aligned} \mathbf{r}_\chi&=\frac{\mathrm{d}\mathbf{S}}{\mathrm{d}\xi}\mathbf{e}/L_0 \\ \mathbf{r}_{\chi\chi}&=\frac{\mathrm{d}^2\mathbf{S}}{\mathrm{d}\xi^2}\mathbf{e}/L_0^2 \end{aligned} \tag{15}$$

Taking partial of Eq. (13) against $\mathbf{e}$ yields the following generalised elastic forces.

$$\mathbf{Q}=\left(\frac{\partial U}{\partial \mathbf{e}}\right)^T=\mathbf{K}_\mathrm{e}\mathbf{e} \tag{16}$$

In this way, the secant element stiffness matrix $\mathbf{K}_\mathrm{e}$ can be generated. In the initialisation procedure, the tangent stiffness matrix is more likely to be used to calculate the incremental nodal DOF vector $\Delta\mathbf{e}$ and the incremental unstrained length ΔL_0. The corresponding tangent stiffness matrices $\mathbf{K}_\mathrm{T}$ and $\mathbf{K}_\mathrm{L}$ can be obtained by taking partial of Eq. (16) against $\mathbf{e}$ and L_0 as follows:

$$\Delta\mathbf{F}=\frac{\partial\mathbf{Q}}{\partial\mathbf{e}}\Delta\mathbf{e}+\frac{\partial\mathbf{Q}}{\partial L_0}\Delta L_0=\mathbf{K}_\mathrm{T}\Delta\mathbf{e}+\mathbf{K}_\mathrm{L}\Delta L_0 \tag{17}$$

A similar derivation can also be used to derive the tangent stiffness matrices of the ANCF cable element. The dropper slackness entails the change of the axial stiffness to zero. Assembling the element matrices yields the global incremental equilibrium equation for the whole catenary as follows:

$$\Delta\mathbf{F}^\mathrm{G}=\mathbf{K}_\mathrm{T}^\mathrm{G}\Delta\mathbf{U}_\mathrm{C}+\mathbf{K}_\mathrm{L}^\mathrm{G}\Delta\mathbf{L}_0 \tag{18}$$

where $\Delta\mathbf{F}^\mathrm{G}$ is the global unbalanced force vector. $\mathbf{K}_\mathrm{T}^\mathrm{G}$ and $\mathbf{K}_\mathrm{L}^\mathrm{G}$ are the global stiffness matrices related to the incremental nodal displacement vector $\Delta\mathbf{U}_\mathrm{C}$ and the incremental unstrained length vector $\Delta\mathbf{L}_0$, respectively. The initial configuration of the catenary can be calculated by solving Eq. (18). The details of the initialisation procedure are discussed in section 4.2.

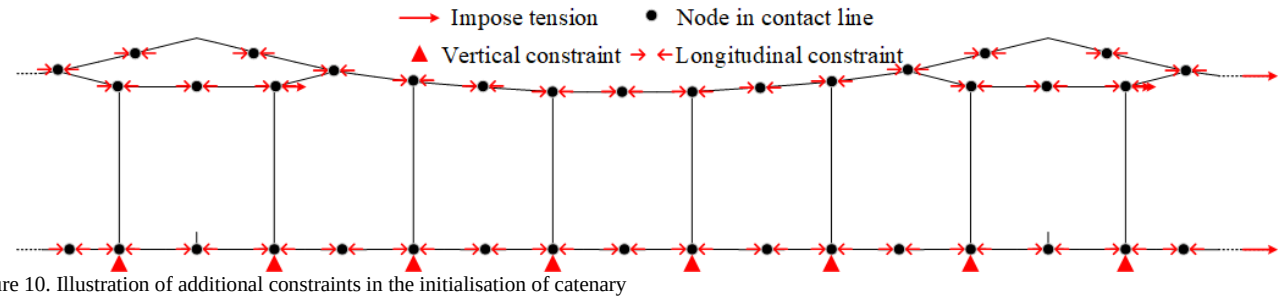

Figure 10. Illustration of additional constraints in the initialisation of catenary

Table 1. Catenary property parameters

Total Length	1.175 km
Contact Line Tension	30 kN
Messenger Line Tension	21 kN
Stitch Line Tension	3.5 kN
Contact Line Area	120 mm^2
Messenger Line Area	120 mm^2
Stitch Line Area	3.44 mm^2
Contact Line Linear Density	1.084 kg/m
Messenger Line Linear Density	0.85 kg/m
Total Number of Spans	24

B. Computation of initial configuration with contact line height variability

In this work, the principle of the TCUD method [34] is adopted to iteratively initialise the catenary, which assumes the undeformed length as unknown parameters, as seen in Eqs. (15-16), and formulate the tangent stiffness matrices $\mathbf{K}_{\mathrm{T}}^{\mathrm{G}}$ and $\mathbf{K}_{\mathrm{L}}^{\mathrm{G}}$. Eq. (16) cannot be solved directly as $\left[\mathbf{K}_{\mathrm{T}}^{\mathrm{G}} \quad \mathbf{K}_{\mathrm{L}}^{\mathrm{G}}\right]$ is not a square matrix. The total number of unknowns exceeds the total number of equations, which leads to undetermined solutions. Therefore, additional constraint conditions should be provided to suppress undesired movements according to design specifications. In this way, $\left[\mathbf{K}_{\mathrm{T}}^{\mathrm{G}} \quad \mathbf{K}_{\mathrm{L}}^{\mathrm{G}}\right]$ can be reduced to a square matrix, which ensures that Eq. (16) has unique solutions. The additional constraint conditions can be classified into three types, as demonstrated in Figure 10:

- The vertical position of the dropper point in the contact line is restricted according to the height of key points;
- The longitudinal direction of each node is restricted to suppress the longitudinal movement;
- The designing tensions are imposed on the endpoints of messenger, contact and stitch lines.

These constraint conditions supply additional equations to reduce the numbers of unknowns in Eq. (16). The equality between the numbers of equations and unknowns ensures a unique solution for the catenary's target configuration. The steady arm points are fixed tentatively in the shape-finding process to place the steady arm points at their correct positions properly. Then, the inclination of each steady arm is determined by the resistance forces in the fixed point, and a rigid truss element replaces the constraint without rotation DOFs to represent a steady arm's realistic behaviour.

An example is presented here using the parameters of a real catenary from the Wuhan-Guangzhou high-speed line. The main parameters of the catenary are presented in Table 1. Using one sample of the time history $\gamma(n)$, as shown in Figure 9 (a), the key point heights can be extracted by the interpolation according to their spatial positions in the design specification. Employing the abovementioned TCUD method, the initialised catenary configuration is presented in Figure 11. The difference between the ideal configuration and the actual configuration when considering contact line height variability can be observed. This model is also used in the following dynamic simulations with double pantographs. Considering the double pantograph spacing and the boundary effect, the central six spans are chosen as the analysis range.

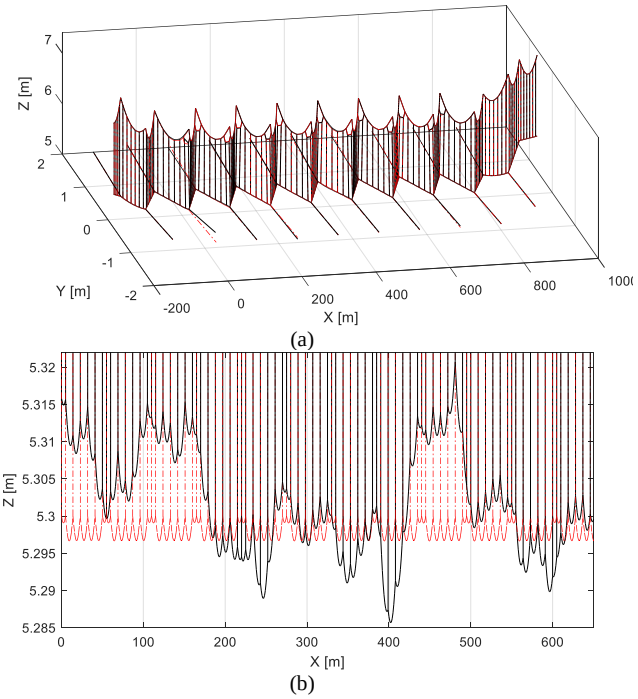

Figure 11. Results of catenary geometry: (a) Full geometry; (b) Contact line height
(Red dash line denotes the ideal configuration; Black line denotes the configuration with contact line height variability)

C. Pantographs-catenary interaction formulation

A lumped mass model is adopted here to represent the pantograph, which can adequately reflect a real one's critical modes. The contact between the two systems is described by a penalty function method. Based on the assumption of the relative penetration between the two contact surfaces, the contact force f_{c} can be calculated by:

$$f_{\mathrm{c}} = \begin{cases} k_{\mathrm{s}}\delta & if\ \delta > 0 \\ 0 & if\ \delta \le 0 \end{cases} \tag{17}$$

in which the penetration δ can be evaluated by

$$\delta = z_1 - z_{\mathrm{c}} \tag{18}$$

where z_1 and z_{c} are the vertical displacements of the pantograph collector and the contact line. Considering a double pantographs' operation, two DSA380 pantographs contact the catenary simultaneously. The interval of two pantographs is defined as 200 m. The equation of motion for the double pantographs-catenary system can be written by

$$\mathbf{M}^{\mathrm{G}}\ddot{\mathbf{U}}(t) + \mathbf{C}^{\mathrm{G}}\dot{\mathbf{U}}(t) + \mathbf{K}^{\mathrm{G}}(t)\mathbf{U}(t) = \mathbf{F}^{\mathrm{G}}(t) \tag{19}$$

in which $\mathbf{M}^{\mathrm{G}}$, $\mathbf{C}^{\mathrm{G}}$ and $\mathbf{K}^{\mathrm{G}}(t)$ are the mass, damping and stiffness matrices for the whole coupled system, respectively. $\mathbf{F}^{\mathrm{G}}(t)$ is the external force vector. Eq. (19) can be solved by a Newmark integration scheme. The stiffness matrix $\mathbf{K}^{\mathrm{G}}(t)$ is updated according to the catenary deformation in each time step to describe both the geometrical and unsmooth nonlinearities fully.

V. Performance Assessment with Contact Line Height Variability

The present catenary model has been validated against the European standard [35], the benchmark [36] and the measured data [37]. The updated catenary model with the contact line height variability and two lumped-mass models of the pantograph are coupled to perform the stochastic analysis and investigate the current collection quality at different speeds. This line's operating speed is 300 km/h, and the design speed is 350 km/h. In the numerical simulation, the train speed is defined as 300 km/h, 325 km/h, 350 km/h and 375 km/h to evaluate the contact force's dispersion caused by the stochastic contact line height. The whole procedure is presented in Figure 12. The pantograph uplift force is taken as the summation of the static contact force and the aerodynamic force. The latter is calculated through CFD (Computational Fluid Dynamics). A CFD model of the pantograph is constructed in ANSYS. Fluent according to its realistic geometry information. Considering the train speeds of 300 km/h and 350 km/h, the flow speed distribution around the pantograph is presented in Figure 13. The resultant lift can be estimated by the summation of the lift on each component via multibody dynamics. The resultant lifts with different train speeds are presented in Figure 14. It is seen that after 3s of simulation, the resultant lifts become stable and no fluctuation can be seen.

According to the assessment standard, the contact force filtered within 0-20 Hz is taken as the assessment index. In this work, the cut-off frequency is improved to 200 Hz to describe the contact loss at high frequencies. The approaches proposed in [32] are adopted here to ensure the simulation results' accuracy at high frequencies. The number of cases is chosen as 500. Comparing the resulting contact force standard deviations with different case numbers indicates that the numerical result becomes stable when the case number is more than 350.

A. *Contact force standard deviation*

First, the contact force standard deviations are analysed as they are the most critical indicator to reflect the fluctuation in contact forces. Based on a Gaussian distribution assumption, the PDF (probability density function) of the contact force standard deviation calculated by 500 simulation results is presented in Figure 15. It is seen that the stochastics of contact line height causes a significant dispersion of the result for each case. Dash-dotted lines denote the ideal results without contact line height variability. For all cases, the mean values of the standard deviation are bigger than the ideal results, which means that the contact line height variability causes the increase of the standard deviation for most cases. Notably, for the trailing pantograph at 300 km/h, the current collection quality in almost all cases is worse than the ideal result after the contact line height variability is introduced. Figure 16 presents the variances of the resulting contact force standard deviation to evaluate the dispersion of the results caused by the contact line height variability. The dispersion of the result undergoes a continuous increase with the speed upgrade. The uncertainty in the result of the trailing pantograph is higher than the leading pantograph. Especially at high speed, the trailing pantograph contact force's uncertainty is much more significant than the leading pantograph.

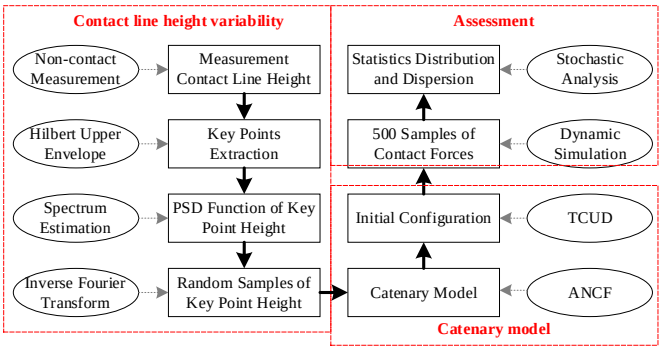

Figure 12. Procedure to implement assessment with contact line height variability

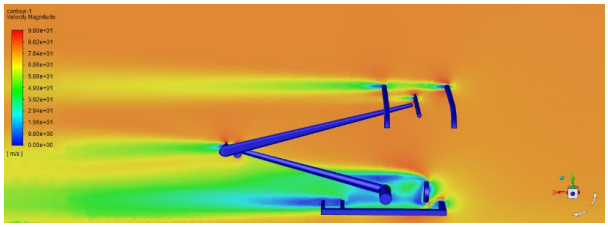

(a)

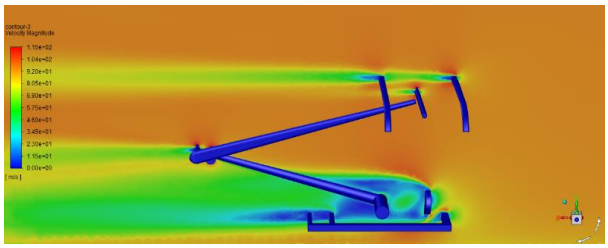

(b)

Figure 13. Flow speed distribution of the pantograph at (a) 300 km/h and (b) 350 km/h

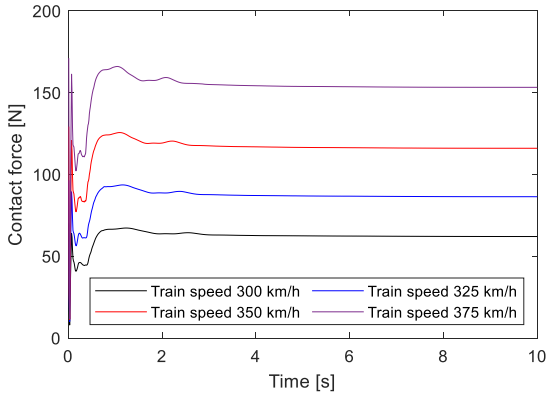

Figure 14. Resultant lift of the pantograph with different train speeds

B. *Maximum contact force*

The maximum contact force is a crucial safety index that should be strictly restricted to avoid the contact line's overlarge stress.

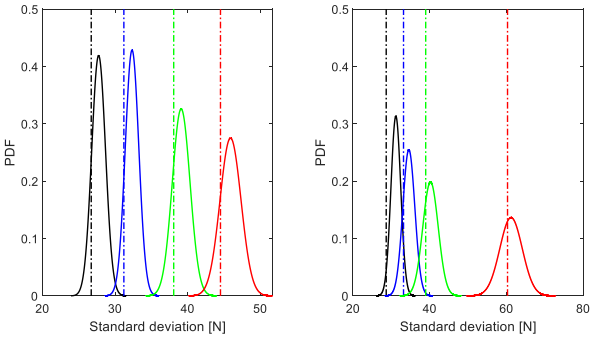

(a) (b)

Figure 15. PDF of contact force standard deviation with 200 Hz cut-off frequency: (a) Leading pantograph; (b) Trailing pantograph
(Red line denotes the results at 375 km/h; Green line denotes the results at 350 km/h; Blue line denotes the results at 325 km/h; Black line denotes the results at 300 km/h; Dash-dotted lines denote the ideal results without contact line height variability)

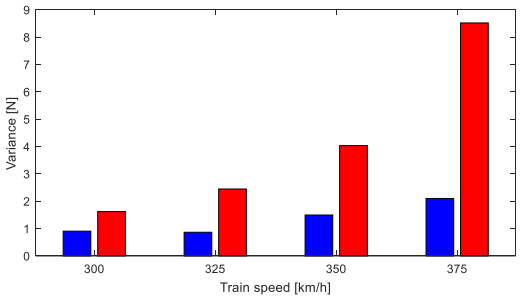

Figure 16. The variance of resulting contact force standard deviation with 200 Hz cut-off frequency
(Blue bar denotes the leading pantograph; Red bar denotes the trailing pantograph)

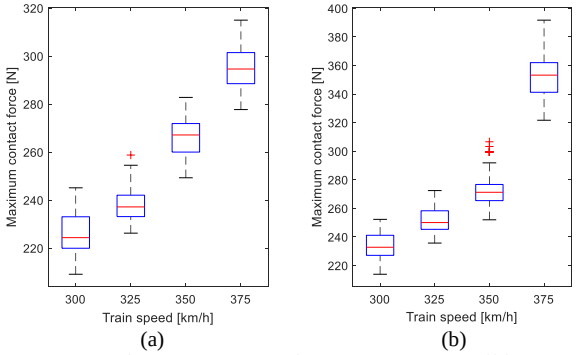

(a) (b)

Figure 17. Boxplot of maximum contact force with 20 Hz cut-off frequency: (a) Leading pantograph; (b) Trailing pantograph

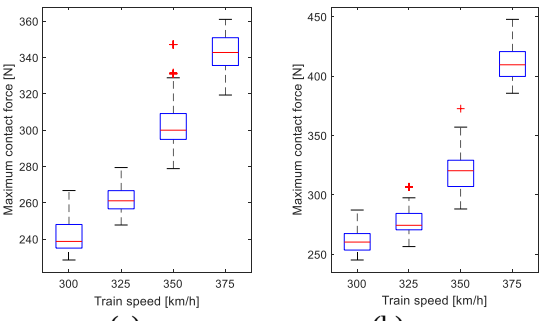

(a) (b)

Figure 18. Boxplot of maximum contact force with 200 Hz cut-off frequency: (a) Leading pantograph; (b) Trailing pantograph

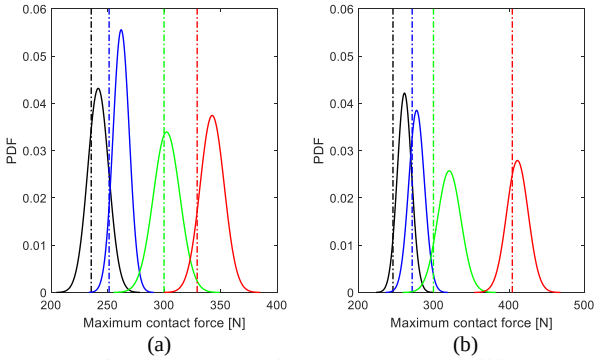

(a) (b)

Figure 19. PDF of maximum contact force with 200 Hz cut-off frequency: (a) Leading pantograph; (b) Trailing pantograph
(Red line denotes the results at 375 km/h; Green line denotes the results at 350 km/h; Blue line denotes the results at 325 km/h; Black line denotes the results at 300 km/h; Dash-dotted lines denote the ideal results without contact line height variability)

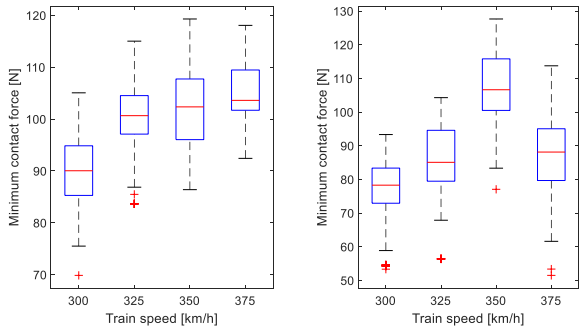

(a) (b)

Figure 20. Boxplot of minimum contact force with 20 Hz cut-of frequency: (a) Leading pantograph; (b) Trailing pantograph

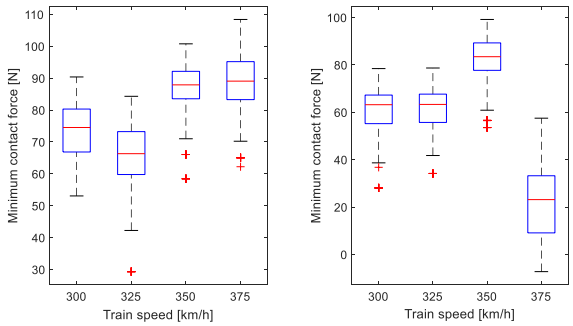

(a) (b)

Figure 21. Boxplot of minimum contact force with 200 Hz cut-off frequency: (a) Leading pantograph; (b) Trailing pantograph

Adopting a 20 Hz cut-off frequency specified in the standard [38], the boxplots of the maximum contact force for the leading and trailing pantographs are presented in Figures 17 (a) and (b), respectively. The increase of the train speed leads to a continuous increase of the maximum contact force. According to the design specification, the maximum contact force should be limited below 350 N to prevent the damage of catenary when the train speed is above 250 km/h. It clears that the trailing pantograph's maximum contact force exceeds the safety threshold when the train speed reaches 375 km/h. It should be noted that the ideal maximum contact force calculated by the numerical simulation with design data is only 344.9 N, which is smaller than the safety threshold. The contact line height

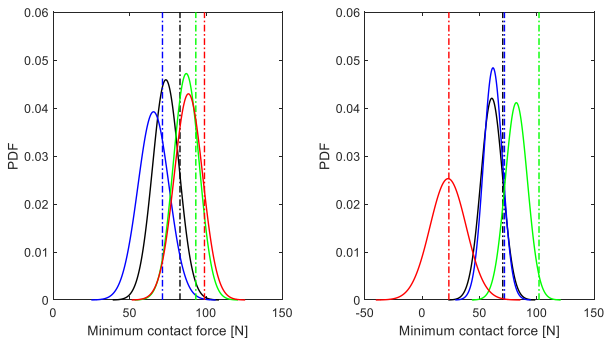

Figure 22. PDF of minimum contact force with 200 Hz cut-off frequency: (a) Leading pantograph; (b) Trailing pantograph
(Red line denotes the results at 375 km/h; Green line denotes the results at 350 km/h; Blue line denotes the results at 325 km/h; Black line denotes the results at 300 km/h; Dash-dotted lines denote the ideal results without contact line height variability)

variability causes the risk of safety accident, which cannot be seen in the ideal result. Therefore, it is essential to take real-life perturbations into account in the design phase of pantograph-catenary.

The boxplots of the maximum contact force with 200 Hz cut-off frequency are presented in Figure 18. Similarly, the increase of the train speed caused the increase of the maximum contact force for both pantographs. It also is seen that the maximum contact force is much more significant with a higher cut-off frequency. The corresponding PDFs are presented in Figure 19. For all cases, the maximum contact force's mean values are bigger than the ideal results, which demonstrates that the contact line height variability causes more risks of a safety accident. The PDFs in Figure 19 can also be used to do the probabilistic analysis and evaluate the reliability. Currently, there is no standard for the maximum contact force at 200 Hz cut-off frequency. Assume that the safety threshold is 420 N for the maximum contact force, which is slightly higher than the ideal maximum contact force at 375 km/h. It can be inferred that the maximum contact force has a 25.89% probability to exceed the safety threshold, and the reliability of the system is 0.74. The high-frequency behaviour still deserves further investigation to propose a more appropriate threshold for the contact force statistics.

When the cut-off frequency increases up to 200 Hz, the minimum contact force's boxplots are presented in Figure 21. The minimum contact force is much smaller with a higher cut-off frequency. Remarkably, some negative minimum contact forces can be seen on the trailing pantograph when the train speed reaches 375 km/h. These negative contact forces are caused by the Fourier filtering algorithm [39], which indicates the occurrences of contact loss at 200 Hz. However, the assessment with the current standard in Figure 20 cannot indicate these contact losses, which definitely leads to a radical result. Therefore, the frequency range of interest in the current standard is desired to be improved to ensure that the potential contact loss caused by real-life disturbances (such as the contact line height variability) can be evaluated in the design phase.

Figures 22 (a) and (b) show the minimum contact force's PDFs with 200 Hz cut-off frequency for both leading and trailing pantographs, respectively. With the help of Figure 22, the reliability of the pantographs-catenary system can be evaluated. At 375 km/h, the trailing pantograph's contact loss has a 7.48% probability to happen. If no contact loss is desired, the system's reliability can reach 0.925 at 375 km/h. Considering that the inevitable contact loss is not intolerant in real-life operation, an appropriate minimum contact force threshold should be suggested in future exploration.

VI. Conclusion

In the current design standard, the numerical simulation tools are widely adopted to check the acceptance of the railway catenary system's design strategy. Nevertheless, the current assessment is generally conducted with the perfect design data, in which no practical errors in operation, installation and maintenance are considered. The direct consequence of the long-term service, mounting errors and inadequate maintenance is the contact line height variability, which shows significant pointwise stochastics and leads to an indeterministic performance of the pantographs-catenary system. In this paper, the measured contact line height data is collected from a newly-built high-speed network in China. The heights of the key point (dropper and steady arm point) in the contact line are extracted using the upper envelope based on the Hilbert transformation. The pointwise stochastics of the key points is properly represented by its PSD function. Based on the Monte Carlo method, 500 samples of the time-history of key point height are generated by inverse Fourier transform. With an advanced initialisation procedure, the contact line height variability is correctly included in the catenary's nonlinear finite element model, which employs ANCF beam elements and small mesh size to sufficiently describe the high-frequency behaviour. Considering a double-pantographs operation, the current collection quality is assessed with a high cut-off frequency. The main conclusions are summarised as follows:

1) The height of the dropper and steady arm points in the contact line shows a symmetric distribution with respect to its mean value, which indicates a stationary process and a periodicity relevant to the span length. The PSD function can be used to represent the pointwise stochastics.

2) Different from the deterministic result obtained by the perfect design data, the contact line height variability causes a significant dispersion of the result. The ideal results evaluated with the perfect design data are generally better than the mean values of the results evaluated with the contact line height variability. The speed upgrade causes a bigger uncertainty of the result, especially for the trailing pantograph.

3) The contact line height variability causes the risk of safety accident, which cannot be observed from the ideal result obtained by the perfect design data or low cut-off frequency. The probabilistic assessment is desired to evaluate the stochastic performance of the pantographs-catenary system with real-life disturbances.

4) The occurrences of contact loss at high cut-off frequencies cannot be pointed out by the traditional assessment method. The frequency range of interest in the current standard is desired to be improved to ensure that the potential contact loss caused by the contact line height variability can be evaluated in the design phase.

The current standard stipulates that the numerical simulation tool can be used to check the acceptance of the

design strategy. The analysis result indicates the necessity to include the inevitable contact line height variability into the assessment to avoid actual operation safety risks. It is also suggested that the numerical simulation tool is desired to have the capacity to describe the high-frequency behaviours at up to 200 Hz, which can capture the contact loss and overlarge contact force caused by the errors. The recommendations can be considered to modify the current assessment standard En 50367. It should be indicated that the case number of 500 may not suffice to describe the stochastics of the contact line height variability entirely. This number is desired to be improved when high-performance computational resources can be accessed. The numerical results' verification is also a technical challenge as the current measurement equipment can only ensure accuracy at up to 20 Hz. Further improvement of the measurement equipment is desired to provide high-frequency measurement data to validate the numerical results.

REFERENCES

[1] Z. Liu, X. Hu, and Y. Liao, "Vehicle-Grid System Stability Analysis Based on Norm Criterion and Suppression of Low-Frequency Oscillation with MMC-STATCOM," *IEEE Trans. Transp. Electrif.*, vol. 4, no. 3, pp. 757–766, 2018.

[2] E. Di Stefano, C. A. Avizzano, M. Bergamasco, P. Masini, M. Menci, and D. Russo, "Automatic inspection of railway carbon strips based on multi-modal visual information," *IEEE/ASME Int. Conf. Adv. Intell. Mechatronics, AIM*, pp. 178–184, 2017.

[3] H. Höfler, M. Dambacher, N. Dimopoulos, and V. Jetter, "Monitoring and inspecting overhead wires and supporting structures," *IEEE Intell. Veh. Symp. Proc.*, pp. 512–517, 2004.

[4] Z. Zhang *et al.*, "Smart Electric Neutral Section Executer Embedded with Automatic Pantograph Location Technique Based on Voltage and Current Signals," *IEEE Trans. Transp. Electrif.*, vol. 6, no. 3, pp. 1355–1367, 2020.

[5] K. Li, Z. Zhang, S. Member, Z. Zhang, and G. S. Member, "Analysis and Correction of a Pantograph Location Method Based on Current Information of Traction Network," *IEEE Trans. Transp. Electrif.*, vol. 7782, no. c, 2021.

[6] Y. Song, Z. Wang, Z. Liu, and R. Wang, "A spatial coupling model to study dynamic performance of pantograph-catenary with vehicle-track excitation," *Mech. Syst. Signal Process.*, vol. 151, p. 107336, 2021.

[7] S. Chen and F. Sha, "Three types of electromagnetic noise between pantograph and catenary," *Proc. - 2009 3rd IEEE Int. Symp. Microwave, Antenna, Propag. EMC Technol. Wirel. Commun. MAPE 2009*, no. 2008, pp. 40–43, 2009.

[8] I. Aydin, M. Karaköse, and E. Akin, "A robust anomaly detection in pantograph-catenary system based on mean-shift tracking and foreground detection," *Proc. - 2013 IEEE Int. Conf. Syst. Man, Cybern. SMC 2013*, pp. 4444–4449, 2013.

[9] Z. Liu, Y. Song, Y. Han, H. Wang, J. Zhang, and Z. Han, "Advances of research on high-speed railway catenary," *J. Mod. Transp.*, vol. 26, no. 1, pp. 1–23, Mar. 2018.

[10] J. Martin, "Dynamic Modelling of Overhead Power Lines for Electric Trains," in *2018 UKACC 12th International Conference on Control, CONTROL 2018*, 2018, pp. 120–125.

[11] Y. Song, Z. Liu, H. Wang, J. Zhang, X. Lu, and F. Duan, "Analysis of the galloping behaviour of an electrified railway overhead contact line using the non-linear finite element method," *Proc. Inst. Mech. Eng. Part F J. Rail Rapid Transit*, vol. 232, no. 10, pp. 2339–2352, 2018.

[12] Y. Song, Z. Liu, F. Duan, X. Lu, and H. Wang, "Study on wind-induced vibration behavior of railway catenary in spatial stochastic wind field based on nonlinear finite element procedure," *J. Vib. Acoust. Trans. ASME*, vol. 140, no. 1, pp. 011010-1–14, 2018.

[13] W. Wei *et al.*, "Study on Pantograph Arcing in a Laboratory Simulation System by High-Speed Photography," *IEEE Trans. Plasma Sci.*, vol. 44, no. 10, pp. 2438–2445, 2016.

[14] D. Feng, Z. He, S. Lin, Z. Wang, and X. Sun, "Risk Index System for Catenary Lines of High-Speed Railway Considering the Characteristics of Time-Space Differences," *IEEE Trans. Transp. Electrif.*, vol. 3, no. 3, pp. 739–749, 2017.

[15] S. B. Gao, Z. G. Liu, and L. Yu, "Detection and monitoring system of the pantograph-catenary in high-speed railway (6C)," in *2017 7th International Conference on Power Electronics Systems and Applications - Smart Mobility, Power Transfer and Security, PESA 2017*, 2018, vol. 2018-Janua, pp. 1–7.

[16] H. Wang *et al.*, "Detection of Contact Wire Irregularities Using a Quadratic Time-Frequency Representation of the Pantograph-Catenary Contact Force," *IEEE Trans. Instrum. Meas.*, vol. 65, no. 6, pp. 1385–1397, 2016.

[17] M. Karakose, O. Yaman, I. Aydin, and E. Karakose, "Real-time condition monitoring approach of pantograph-catenary system using FPGA," *IEEE Int. Conf. Ind. Informatics*, vol. 0, pp. 481–486, 2016.

[18] E. Karakose, M. T. Gencoglu, M. Karakose, I. Aydin, and E. Akin, "A new experimental approach using image processing-based tracking for an efficient fault diagnosis in pantograph-catenary systems," *IEEE Trans. Ind. Informatics*, vol. 13, no. 2, pp. 635–643, 2017.

[19] F. Vesali, M. A. Rezvani, H. Molatefi, and M. Hecht, "Static form-finding of normal and defective catenaries based on the analytical exact solution of the tensile Euler–Bernoulli beam," *Proc. Inst. Mech. Eng. Part F J. Rail Rapid Transit*, vol. 233, no. 7, pp. 691–700, 2019.

[20] Y. Song, Z. Liu, and X. Lu, "Dynamic Performance of High-Speed Railway Overhead Contact Line Interacting with Pantograph Considering Local Dropper Defect," *IEEE Trans. Veh. Technol.*, vol. 69, no. 6, pp. 5958–5967, 2020.

[21] D. Song, Y. Jiang, and W. Zhang, "Dynamic performance of a pantograph–catenary system with consideration of the contact surface," *Proc. Inst. Mech. Eng. Part F J. Rail Rapid Transit*, vol. 232, no. 1, pp. 262–274, 2018.

[22] Y. Song, P. Antunes, J. Pombo, and Z. Liu, "A methodology to study high-speed pantograph-catenary interaction with realistic contact wire irregularities," *Mech. Mach. Theory*, vol. 152, no. xxxx, p. 103940, May 2020.

[23] Y. Song *et al.*, "Contact Wire Irregularity Stochastics and Effect on High-Speed Railway Pantograph-Catenary Interactions," *IEEE Trans. Instrum. Meas.*, vol. 69, no. 10, pp. 8196–8206, Oct. 2020.

[24] S. Gregori, M. Tur, J. E. Tarancón, and F. J. Fuenmayor, "Stochastic Monte Carlo simulations of the pantograph–catenary dynamic interaction to allow for uncertainties introduced during catenary installation," *Veh. Syst. Dyn.*, vol. 57, no. 4, pp. 471–492, 2019.

[25] O. V. Van, J. P. Massat, C. Laurent, and E. Balmes, "Introduction of variability into pantograph-catenary dynamic simulations," *Veh. Syst. Dyn.*, vol. 52, no. 10, pp. 1254–1269, 2014.

[26] Z. Xu, Y. Song, and Z. Liu, "Effective Measures to Improve Current Collection Quality for Double Pantographs and Catenary Based on Wave Propagation Analysis," *IEEE Trans. Veh. Technol.*, vol. 69, no. 6, pp. 6299–6309, 2020.

[27] W. Zhai, *Vehicle–Track Coupled Dynamics*. Springer Singapore, 2020.
[28] B. Bhardwaj, R. Bridgelall, L. Chia, P. Lu, and N. Dhingra, "Signal Filter Cut-Off Frequency Determination to Enhance the Accuracy of Rail Track Irregularity Detection and Localization," *IEEE Sens. J.*, vol. 20, no. 3, pp. 1393–1399, 2020.
[29] Z. Wang, Y. Song, Z. Yin, R. Wang, and W. Zhang, "Random Response Analysis of Axle-Box Bearing of a High-Speed Train Excited by Crosswinds and Track Irregularities," *IEEE Trans. Veh. Technol.*, vol. 68, no. 11, pp. 10607–10617, 2019.
[30] L. Wang, Z. Deng, H. Wang, H. Li, K. Li, and S. Ma, "Dynamic Responses of HTS Maglev System under Track Random Irregularity," *IEEE Trans. Appl. Supercond.*, vol. 30, no. 4, Jun. 2020.
[31] P. Olga, P. Alexey, and S. Natalia, "Hilbert Envelope Extraction from Real Discrete Finite Signals Considering the Nonlocality of Hilbert Transform," *2020 22th Int. Conf. Digit. Signal Process. its Appl. DSPA 2020*, vol. 2, no. 5, pp. 2–5, 2020.
[32] Y. Song *et al.*, "Assessment of the High-Frequency Response in Railway Pantograph-Catenary Interaction Based on Numerical Simulation," *IEEE Trans. Veh. Technol.*, vol. 69, no. 10, pp. 10596–10605, 2020.
[33] J. Ambrósio, J. Pombo, M. Pereira, P. Antunes, and A. Mósca, "Recent Developments in Pantograph-Catenary Interaction Modelling and Analysis," *Int. J. Railw. Technol.*, vol. 1, no. 1, pp. 249–278, 2012.
[34] Y. Song, Z. Liu, Z. Xu, and J. Zhang, "Developed moving mesh method for high-speed railway pantograph-catenary interaction based on nonlinear finite element procedure," *Int. J. Rail Transp.*, vol. 7, no. 3, pp. 173–190, 2019.
[35] European Committee for Electrotechnical Standardization, *EN 50317: Railway applications - Current collection systems - Requirements for and validation of measurements of the dynamic interaction between pantograph and overhead contact line*. Brussels: European Standards (EN), 2012.
[36] S. Bruni *et al.*, "The results of the pantograph-catenary interaction benchmark," *Veh. Syst. Dyn.*, vol. 53, no. 3, pp. 412–435, Mar. 2015.
[37] Y. Song, Z. Liu, F. Duan, Z. Xu, and X. Lu, "Wave propagation analysis in high-speed railway catenary system subjected to a moving pantograph," *Appl. Math. Model.*, vol. 59, pp. 20–38, 2018.
[38] European Committee for Electrotechnical Standardization, *EN 50367. Railway applications — Current collection systems — Technical criteria for the interaction between pantograph and overhead line.* Brussels: European Standards (EN), 2012.
[39] F. Transforms, "13 . 5 Digital Filtering in the Time Domain," *Digit. Signal Process.*, pp. 551–557, 1989.

Yang Song (S'16–M'19) received a Ph.D. degree from Southwest Jiaotong University, Chengdu, China, in 2018. He is currently a postdoctoral fellow in the Department of Structural Engineering, Norwegian University of Science and Technology. His research interests involve the assessment of railway pantograph-catenary interactions, the wind-induced vibration of long-span structures in railway transportation.

Fuchuan Duan (Student Member, IEEE) received a Ph.D. degree from School of Electrical Engineering, Southwest Jiaotong University, Chengdu, China, in 2021. He is currently postdoctoral fellow in Institute of Rail Transit, Tongji University, Shanghai, China. His research interests include finite-element modelling, structural dynamics, image processing, and their applications in the design and maintenance of railway pantograph–catenary system.

Fanping Wu (S'15-J'19) received a B.S. degree from Southwest Jiaotong University, Chengdu, China, in 2019. He is currently pursing his master degree at School of Electrical Engineering, Southwest Jiaotong University. His research interest is the wind induced vibration response of pantograph catenary system in canyon wind.

Zhigang Liu (M'06–SM'16) received a Ph.D. degree in power system and its automation from the Southwest Jiaotong University, Sichuan, China, in 2003. He is currently a Full Professor with the School of Electrical Engineering, Southwest Jiaotong University, China. His current research interests include the electrical relationship of vehicle-grid in high-speed railway, pantograph-catenary interaction, and status assessment. Prof. Liu was awarded the fellowship of the Institute of Engineering and Technology in 2017. He is an Associate Editor of the IEEE Transactions on Instrumentation and Measurement, IEEE Transactions on Vehicular Technology and IEEE Access.

Shibi Gao received the B.S., M.S., and Ph.D. degrees in electrical engineering from Southwest Jiaotong University, Chengdu, China, in 1986, 1999, and 2004, respectively. Currently, He is a Professor and doctoral supervisor in the School of Electrical Engineering, Southwest Jiaotong University. His research interests include the analysis of power supply system, relay protection, and integrated automation in traction power supply system.